Insight into the Contact Mechanism of Ag/Al–Si Interface for the Front-Side Metallization of TOPCon Silicon Solar Cells

Yongsheng Li, Rui Zhou, Ziwei Chen, Yuhang Li, Xing Cheng, Bo Zhang, Jun Chen, Yuan Lin,* and Feng Pan**

For N-type tunnel-oxide-passivated-contact silicon solar cells, optimal Ag/Al–Si contact interface is crucial to improve the efficiency. However, the specific roles of Ag and Al at the interface have not been clearly elucidated. Hence, this work delves into the sintering process of Ag/Al paste and examines the impact of the Ag/Al–Si interface structure on contact quality. By incorporating TeO_2 into PbO-based Ag/Al paste, the Ag/Al–Si interface structure can be modulated. It can be found that TeO_2 accelerates the sintering of Ag powder and increases Ag colloids within glass layer, while it simultaneously impedes the diffusion of molten Al. It leads to a reduced Al content near the Ag/Al–Si interface and a shorter diffusion distance of Al into Si. Notably, it can be demonstrated that the diffusion of Al in Si layer is more effective to reduce the contact resistance than the precipitation of Ag colloids. Therefore, the PbO-based Ag/Al paste, which favors Al diffusion, leads to solar cells with lower contact resistance and series resistance, higher fill factor, and superior photoelectric conversion efficiency. In brief, this work is significant for optimizing metallization of silicon solar cells and other semiconductor devices.

1. Introduction

Crystalline silicon (c-Si) solar cells have become the main technology in the photovoltaics industry. Presently, improving photoelectric conversion efficiency (*PCE*) and reducing costs are still the goals of photovoltaic technology development.[1] One of the major challenges in c-Si solar cells is the high series resistance (*Rs*) caused by high contact resistance (*Rc*), which poses a significant barrier to efficient carrier extraction, ultimately affecting the photoelectric conversion efficiency (PCE) of devices. This is because the quality of the metal–semiconductor contact determines the contact resistance.[2] In N-type tunnel oxide passivated contact (TOPCon) solar cells, silver (Ag) paste and silver/aluminum (Ag/Al) paste are utilized to establish metal–semiconductor contacts on the rear and front-side of the devices, respectively, with the aim of enhancing carrier collection efficiency. Specifically, Ag paste is predominantly employed to create an Ag–Si contact for the n^+ emitter of these devices.[3] On the contrary, the lack of electrons at the p^+ emitter makes it difficult to form good Ag–Si contact by using Ag paste.[4] The utilization of Ag/Al paste is attributed to the formation of specific metallic spikes through the addition of Al powder, a feature that significantly reduces the R_c.[5] There are numerous studies on Ag–Si contact for n^+ emitter, whereas research on Ag/Al–Si for p^+ contact remains incomplete and lacks in-depth analysis. Hence it is crucial to investigate the sintering process of Ag/Al paste and examine the impact of various Ag/Al–Si interface structures on the electrical characteristics of these contacts.

Ag paste consists of Ag powder, glass frit and organic vehicle, while Ag/Al paste consists of Ag powder, Al powder, glass frit and organic vehicle.[3,5a,b] Glass frits, comprising diverse oxides as functional additives, play a pivotal role in interface formation. They significantly influence not only the sintering of Ag and Al powders but also the etching of the silicon nitride (SiN_x) layer, thus exerting a comprehensive effect.[6] The glass frit of Ag paste generally contain lead oxide (PbO).[7] During the sintering process, PbO in the glass frit reacted with the SiN_x layer and improved the growth of Ag crystalline at the Ag–Si interface so that form Ag-Si contact.[6] In order to optimize the n^+-emitter-specific

---

Y. Li, R. Zhou, Z. Chen, F. Pan
School of Advanced Materials
Shenzhen Graduate School
Peking University
Shenzhen 518055, China
E-mail: panfeng@pkusz.edu.cn

Y. Li, X. Cheng
Tsinghua Shenzhen International Graduate School
Tsinghua University
Shenzhen 518055, China

B. Zhang
State Grid Fujian Electric Power Research Institute
Fuzhou 350007, China

J. Chen
Institute of Zhejiang University-Quzhou
Quzhou 324000, China
E-mail: qiujinchen@zju.edu.cn

Y. Lin
Key Laboratory of Photochemistry
Institute of Chemistry
Chinese Academy of Sciences
Beijing 100190, China
E-mail: linyuan@iccas.ac.cn

The ORCID identification number(s) for the author(s) of this article can be found under https://doi.org/10.1002/smtd.202400707

DOI: 10.1002/smtd.202400707

Ag paste, tellurium dioxide (TeO_2) is incorporated. It promotes the sintering of Ag powder and enhances the precipitation of Ag colloids within the glass layer situated between the Ag and silicon interface. This manipulation of the interface structure effectively reduces the R_c, ultimately leading to an improvement in the PCE.[6,8] In Ag/Al paste, the glass frit usually consists of PbO, SiO_2 and B_2O_3.[4a] The addition of Al powder in the Ag/Al paste leads to distinct sintering and contact formation processes compared to traditional Ag paste. Consequently, the sintering process and interface structure become more intricate. Previous research has found that PbO-based glass frit with low viscous made the sintered body of Ag/Al paste dense, reducing the resistance of the Ag/Al fingers.[4a] Changing the particle size and content of Al powder can modulate the dimensions of the metallic spikes, thereby influencing the quality of the contact interface.[5b] Additionally, Al will induce the variation of Ag crystal orientation during firing.[5c] However, various types of contact structure were discovered and the mechanism of Ag/Al–Si contact have not been clearly elucidated.[9] Therefore, it is urgent to clarify the roles of Ag and Al at the Ag/Al–Si interface.

In order to explore the influence of Ag and Al on the Ag/Al–Si contact, it is essential to regulate the sintering process of the Ag/Al paste and the Ag/Al–Si interface structure. Inspired by previous researches, TeO_2 was employed to control the speed of Ag powder sintering and adjust the Ag/Al–Si interface structure. In this work, PbO-based (TeO_2-free) Ag/Al paste and TeO_2-containing Ag/Al paste were prepared, and an in-depth examination was conducted to understand the sintering process and discern the distinctions in the contact formation mechanism between the two types of pastes. It was found that TeO_2 accelerated the sintering of Ag powder, which made the Ag/Al finger denser and resulted in the high concentration of Ag colloids within the glass layer between Si layer and finger bulk, while the diffusion of Al was hindered. However, the diffusion of Al into Si layer proves to be more effective in reducing R_c compared to the Ag colloids present at the interface. Hence, the reduced Al diffusing into Si layer resulted in poorer contact quality. The differences in electrical performance can be well explained by the characterization results. This work supplements the roles of Al and Ag in Ag/Al paste and reveals the effect of different Ag/Al–Si structures on the contact quality, which is of great significance for the optimization of advanced Ag/Al pastes and the improvement of metallization processes.

2. Result and Discussion

2.1. Manufacture and Performance Characterization of TOPCon Solar Cells

TOPCon solar cells were fabricated using the N-type cells manufacturing process. **Figure** 1a illustrates the Ag/Al paste and devices fabrication process. Ag powder, Al powder and PbO-based glass frit were commercial materials and the SEM images of them were shown in Figure 1b–d. The size of Ag powder is ≈2 µm, and of Al powder ranges from 1–3 µm. The Glass frit is irregular block of 2–4 µm, and the TeO_2 powder is irregular block of 1–4 µm (in Figure S1, Supporting Information). The real device photograph of the TOPCon solar cells in this work was shown in Figure 1e, with Ag/Al fingers on the front and rear Ag fingers (made by commercial materials) on the back. Transmission Line Model (TLM) has been widely used to evaluate the quality of contact.[10] Figure 1f displays the TLM in this work to measure R_c and specific contact resistance (ρ_c). Cell-Pb and Cell-Te were manufactured using P-Pb and P-Te, respectively (the detailed explanation of P-Pb and P-Te is in the Experimental Section (Material Synthesis)). The comparison of the performance parameters of Cell-Pb and Cell-Te is directly presented by a radar chart in Figure 1g. It is evident that Cell-Pb outperformed Cell-Te in multiple aspects, with higher values for open circuit voltage (V_{oc}), short-circuit current density (J_{sc}), fill factor (FF), and PCE (shown in Table S1, Supporting Information). The R_s of Cell-Pb is ≈2.2338 ± 0.147 Ω lower than Cell-Te (≈2.8755 ± 0.137 Ω), and the parallel resistance (R_{sh}) of Cell-Pb is ≈349.1 ± 74.3 Ω higher than Cell-Te (≈205.0 ± 19.6 Ω, in Figure 1h). Figure 1i shows that the contact made by P-Pb has lower R_c (≈0.984 ± 0.076 Ω) and ρ_c (≈0.0706 ± 0.0115 Ω^*cm^2), while P-Te has higher R_c (≈1.354 ± 0.165 Ω) and ρ_c (≈0.1451 ± 0.0375 Ω^*cm^2). R_s, R_{sh}, R_c and ρ_c are mean values of statistical data. Therefore, it can be confirmed that the difference in inorganic composition of the Ag/Al paste causes differences in the front contact, resulting in a difference in their electrical parameters. Additionally, as the content of TeO_2 continues to increase, the R_s of the cells increases (shown in Table S2, Supporting Information), indicating that TeO_2 caused deterioration of Ag/Al–Si contact.

2.2. Comparison of Sintering Process Between P-Pb and P-Te

To understand the sintering process and mechanism of contact formation for Ag/Al paste, the sintered fingers made by P-Pb and P-Te at different temperatures (the peak temperatures are 760 and 810 °C, respectively) were studied.

For P-Pb, **Figure** 2a shows that sintered necks formed between the Ag powder without stepped structure after sintering at 760 °C. In addition, there are many voids in the sintered body (shown in Figure 2b), and Al rarely diffused (the black parts circled in red in Figure 2c) due to the AlO_x shell on the surface of the Al powder. After sintering at 810 °C, the finger still retains many voids (in Figure 2d), but the Al powder in the black part has almost disappeared. Meanwhile, the Ag–Al alloy is present (the light gray parts circled in blue in Figure 2e). The results of EDS show that the molten glass frit diffused throughout the entire sintered body (in Figure S2, Supporting Information). On the one hand, it is beneficial for the contact between the molten glass frit and the Al powder. On the other hand, the molten glass frit could damage the AlO_x shell on the surface of the Al powder, causing the molten Al liquid to flow out and diffuse to the Ag phase and Ag/Al–Si interface.

For P-Te, because TeO_2 can accelerate the sintering of Ag powder, the sintered finger exhibits facets at a lower temperature (760 °C) and the sintered finger is denser than that formed by P-Pb at 810 °C(as shown in Figure 2g–j).[7] After sintering at 810 °C, the Ag–Al alloy appears, while the Al powder still exists obviously in the finger (the black parts circled in red in Figure 2k). Figure S2 (Supporting Information) indicates that the diffusion range of Al in P-Te is relatively small, which confirms the inhibitory effect of TeO_2 on Al diffusion. In addition, there is less Al near the Ag/Al–Si interface for Cell-Te compared to Cell-Pb. This is due

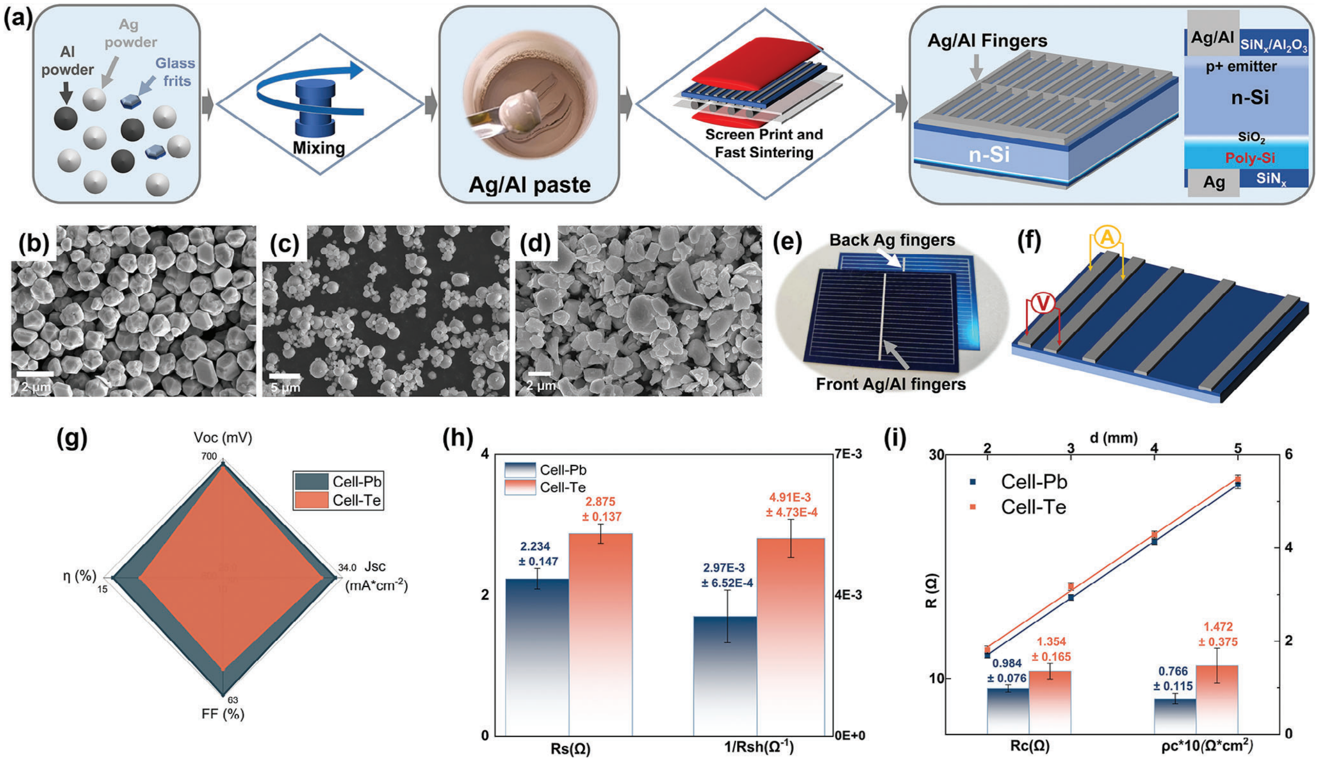

Figure 1. Manufacturing process and characterization of Ag/Al paste and TOPCon solar cell. a) Schematic of the Ag/Al paste and TOPCon solar cells fabrication process and the structural diagram of the device prepared in this work. Left to Right: Ag powder, Al powder and glass frit mixed to prepare Ag/Al paste, followed by screen printing and rapid sintering to manufacture the TOPCon solar cells; SEM images of b) Ag powders, c) Al powders and d) PbO-based glass frit; e) actual photo of the TOPCon cells in this work; f) schematic of TLM method in this work; g) radar chart of performance comparison for cells; h) R_s and R_{sh} and i) R_c and ρ_c of cells (data presented as mean ± SD, n = 5, P-values are calculated using one-way ANOVA with Tukey correction, $p<0.05$).

to the differences in the interaction of inorganic oxide additives with Ag powder and with Al powder, respectively, causing differences in the Ag/Al–Si interface, thereby affecting the electrical performance of the devices.

The mechanisms of distinct actions are depicted in Figure 2f,l. Figure 2f illustrates how, during the sintering process for P-Pb, the molten mixture consisting of glass frit, Al, and Ag flows toward the Ag/Al–Si interface through the Ag/Al finger channels. Conversely, for P-Te, TeO_2 accelerates the densification of the Ag/Al fingers and impedes the flow of the molten mixture toward the Ag/Al–Si interface, as depicted in Figure 2l.

2.3. Influence of Ag/Al–Si Interface Structure on Electrical Characteristics

Due to the addition of TeO_2, which changed the sintering behavior of the Ag/Al paste and thereby impacted interface structure, it is necessary to conduct in-depth research on Ag/Al–Si interface and the effect of its structure on electrical performance.

The structure, element distribution and valence state of the Ag/Al–Si interface of Cell-Pb and Cell-Te (sintered at the optimal peak temperature of 860 °C) were characterized. For Cell-Pb, the glass layer between Si and Ag layer contains few Ag colloids, as shown in **Figure** 3a. Figure 3b–d displays the SEM images and the EDS mapping results obtained from the front metallization area (below the Ag/Al finger) of Cell-Pb. It can be seen that the distribution of Ag (in blue) and Al (in green) on the etched surface is similar, and the ratio of Ag content to Al content is ≈1.75:1 (in Figure S5, Supporting Information). On the contrary, there are numerous Ag colloids in the glass layer between Si and Ag layer for Cell-Te (in Figure 3g). This is due to the fact that TeO_2 increased the Ag solubility within molten glass frit, which corresponds to these large Ag particles on the etched surface in Figure 3h. In addition, the ratio of Ag to Al content is ≈3.89:1, corresponding a strong signal of Ag and a weak signal of Al, as illustrated in Figure 3i,j and Figure S6 (Supporting Information). The above results indicate that there is more Al at the Ag/Al–Si interface for Cell-Pb compared to Cell-Te. To identify the existence forms of Ag and Al at the interface, XPS analysis was performed on the etched surfaces of Cell-Pb and Cell-Te, revealing the elemental valence states depicted in Figure 3e,f,k,l, respectively. The Ag $3d_{5/2}$ peaks can be divided into two peaks, indicating the presence of Ag in two valence states. The higher binding energy peak is 369.0±0.2 eV, which can be classified as Ag–Al alloy.[11] And the lower one is ≈368.3 ± 0.2 eV, Corresponding to Ag.[12] The Al 2p peaks of Cell-Pb and Cell-Te are both 74.6±0.2 eV, which is in Al_2O_3/Al.[12] The Al_2O_3 here may come from the glass layer. The above results combine with the semi-quantitative analysis in Table S3 (Supporting Information), prove that Ag–Al alloy exists on the Ag/Al–Si interface both of Cell-Pb and Cell-Te. However, the difference is the account of Ag–Al alloy in Cell-Pb is

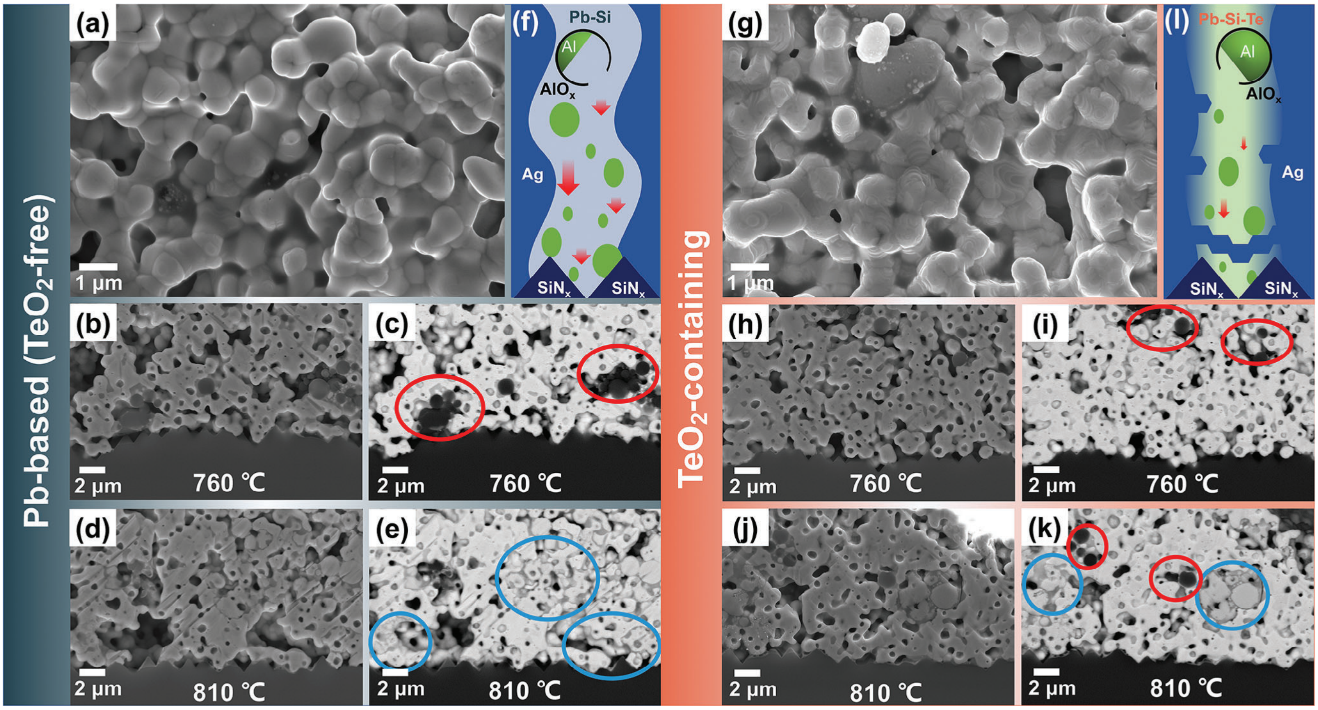

Figure 2. Surface and cross-sectional SEM micrographs of Ag/Al fingers and schematic diagrams of Al diffusion to the Ag/Al–Si interface. Surface micrographs of Ag/Al fingers made by the a) P-Pb and g) P-Te after sintering at 760 °C; cross-sectional micrographs of b–e) P-Pb and h–k) P-Te in secondary electron mode and backscattered electrons mode after sintering at 760 and 810 °C; schematic diagram of Al diffusion during sintering process of f) P-Pb and l) P-Te.

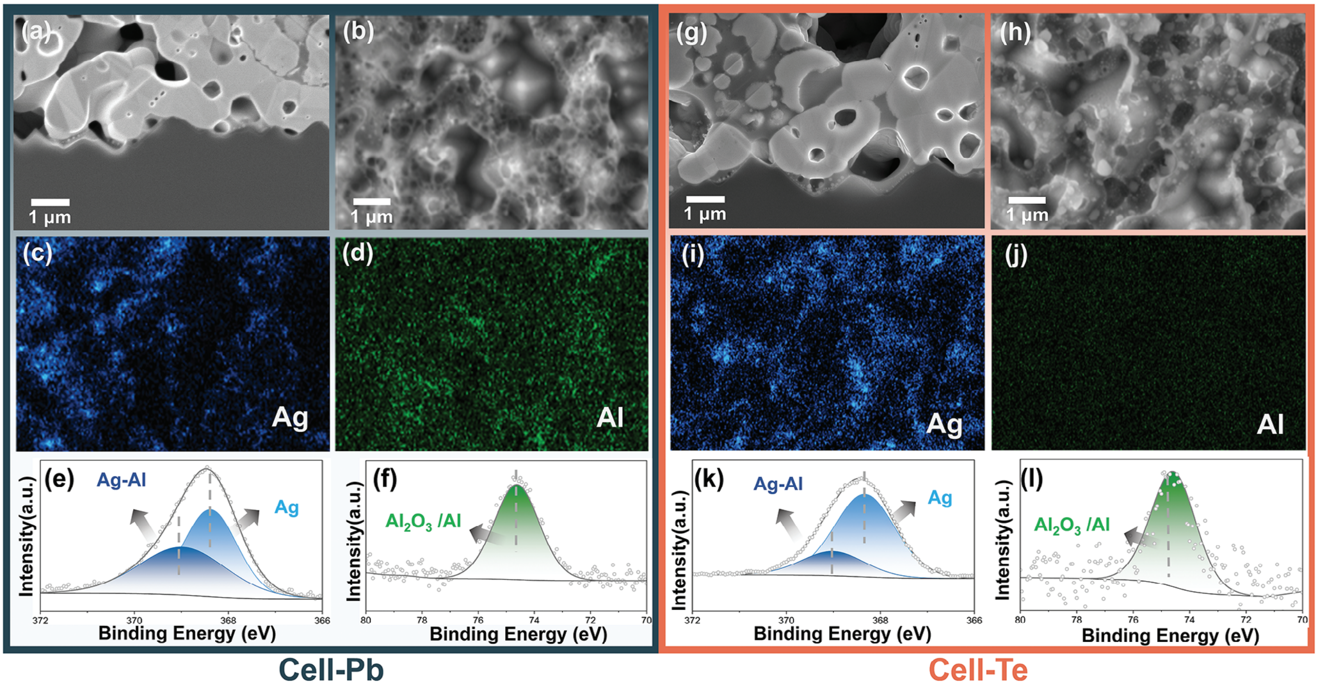

Figure 3. Characterizations of the Ag/Al–Si interface of Cell-Pb and Cell-Te. Cross-sectional interface micrographs of a) Cell-Pb and g) Cell-Te; top micrographs after removing Ag/Al fingers by HNO_3 and ultrasound, with the elements distribution of b–d) Cell-Pb and h–j) Cell-Te; XPS results of the top area on Ag/Al–Si interface of e,f) Cell-Pb and k,l) Cell-Te.

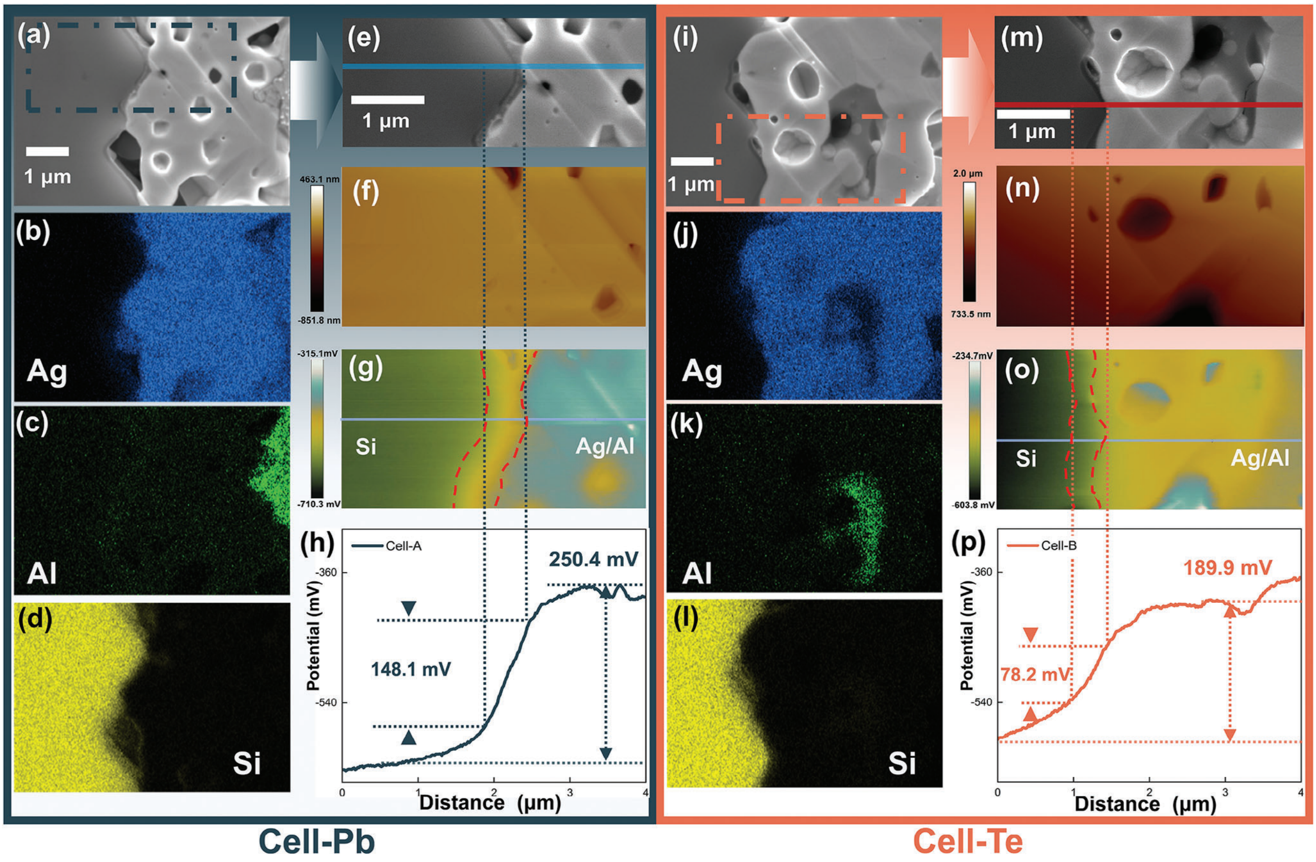

Figure 4. Cross-sectional morphology, EDS mapping, topography, surface potential images and surface potential line profiles of cells. Cross-sectional morphology and EDS mapping of a–d) Cell-Pb and i–l) Cell-Te. Topography, surface potential images and surface potential line profiles of e–h) Cell-Pb and m–p) Cell-Te.

greater than in Cell-Te. By integrating the results from EDS and XPS analyses, it can be indicated that Cell-Pb exhibits a significantly higher proportion of Al alloy at the Ag/Al–Si interface in comparison to Cell-Te.

To further characterize the differences between Cell-Pb and Cell-Te and understand the effect of varying interface structures on electrical performance, the surface potential of the Ag/Al–Si interface was analyzed using Kelvin probe force microscopy (KPFM). **Figure** 4a–d presents the cross-sectional morphology and elements distribution of Cell-Pb, and Figure 4e–g shows the corresponding SEM, topography and surface potential images. Based on these images, distinct regions corresponding to Ag/Al layer, glass layer with Ag/Al–Si diffusion area (the yellow area circled by a red dashed line between Ag and Si) and Si layer can be clearly identified. The contact quality impacts carrier (hole) collection, thereby altering hole redistribution at the interface. This result in a built-in electric field and a gradient in hole density, causing a surface potential step between Si layer and Ag/Al layer. And the higher the surface potential step is, the better the contact will be.[13] Figure 4h present the surface potential curves across these layers. From the Si layer to the Ag layer the surface potential constantly increases. There is a total surface potential step between the Ag layer and the Si layer, with a magnitude of ≈250.4 mV. It is worth noting that the surface potential step of the Ag/Al–Si diffusion layer (with a thickness of 0.71 μm) is ≈148.1 mV, and the rate of potential change is highest in the entire curve (≈209.2 mV μm^{-1}). Figure 4i–o shows the morphology, element distribution, and potential images of Cell-Te, for comparison with Cell-Pb. It is evident that the Al signal on the Ag/Al–Si interface is relatively weaker than Cell-Pb, and the thickness of the Ag/Al–Si diffusion layer is ≈0.51 μm. According to the potential curves in Figure 4p, the change rate in this layer is 152.1 mV μm^{-1}, and the total surface potential step of Cell-Te is 189.9 mV. The higher surface potential step in Cell-Pb compared to Cell-Te indicates that Cell-Pb has better contact quality,[13a] manifesting in the lower R_s, R_c and ρ_c values and higher V_{oc} and J_{sc}. This indicates that the effect of Ag colloids on optimizing the Ag/Al-Si contact is not as significant as the diffusion of Al at the interface.

The FIB was used to prepare samples of cells for TEM in order to deeply investigate the Ag/Al–Si interface structure. **Figure** 5a–d displays the Ag/Al–Si interface structure and elements distribution of Cell-Pb. It can be seen that there are a few Ag colloids close to Ag/Al layer within the glass layer. On the contrary, there are many Ag colloids in the glass layer between the Ag layer and the Si layer for Cell-Te (in Figure 5h–k). The high-resolution TEM (HRTEM) images with the fast Fourier transform (FFT) image confirm this result (in Figure 5e,i, with low magnification images shown in Figure S7, Supporting Information). This is attributed to TeO_2 increasing the Ag solubility in

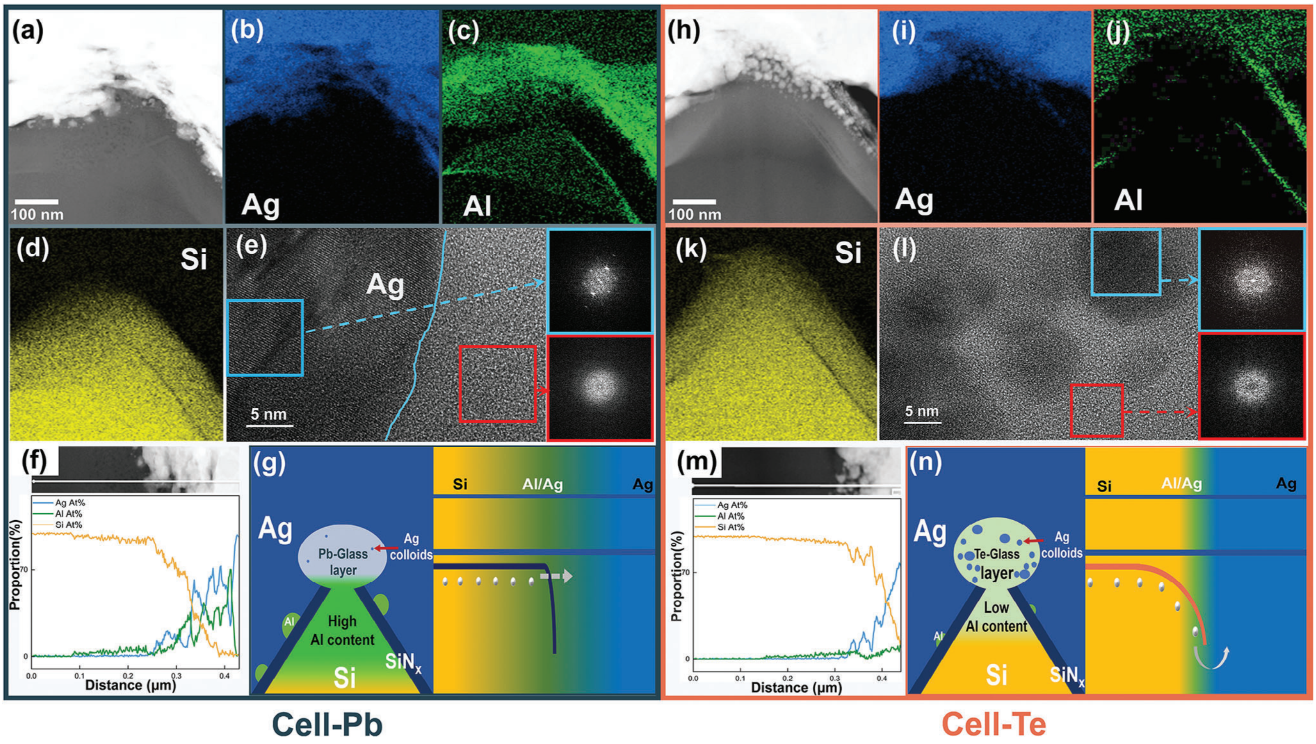

Figure 5. Results of Ag/Al–Si interface morphology with EDS mapping and line scanning by TEM and schematic diagrams of energy band structure of cells. TEM image with EDS mapping of a–d) Cell-Pb and h–k) Cell-Te; HRTEM image with FFT images of the Ag-glass layer for e) Cell-Pb and i) Cell-Te; atomic ratio from EDS line scanning of f) Cell-Pb and m) Cell-Te; schematic diagrams of the two structures and heavily doped energy bands of Ag/Al–Si interface for g) Cell-Pb and n) Cell-Te.

the glass frit.[8b] A larger amount of Ag dissolved into the glass frit, and then, during the cooling process, Ag precipitated at the Ag/Al–Si interface as Ag colloids.[14,15] It should be pointed out that, both to Cell-Pb and Cell-Te, Ag hardly entered the silicon layer, but Al (in green) was gathered near the Ag/Al–Si interface and diffused into the Si layer. To further characterize the differences in the distribution and ratio of elements, the EDS line scanning was used at the Ag/Al-Si interface. Figure 5f shows the EDS line scanning result of Cell-Pb. The regions from left to right correspond to the Si layer, Ag/Al–Si interface, and Ag layer, respectively. Ag only exists at the interface and did not diffuse into the Si layer. The average atomic ratio of Al at the interface is ≈20.63% and in Si layer is ≈3.98%. Starting from the point where the Ag content is ≈0%, the diffusion depth of Al in the silicon layer is ≈170 nm. However, the Al content of Cell-Te is lower than that of Cell-Pb (in Figure 5m), both at the interface (≈6.88%) and in the silicon layer (2.78%). Additionally, the Al diffusion depth of Cell-Te is ≈150 nm, lower than that of Cell-Pb. Previous study indicated that the presence of holes in the p^+ emitter hinders the reduction of Ag^+ to Ag dendrites due to the inability to efficiently acquire electrons, thereby leading to the formation of poor contacts.[16] But, adding Al can help form a good contact and reduce R_c.[17] In the study of metallization using Al paste (back metallization for p-type solar cells), it was found that the diffusion of Al in silicon is beneficial for reducing R_c.[18] Heavy doping of silicon is beneficial for reducing the resistance of carrier transport. In addition, the diffusion of Al creates heavy doping, narrowing the barrier width and thus enabling a low-resistance ohmic contact.[2c,13c,14,19] Figure 5g,n illustrates schematic diagrams of the two structures and heavily doped energy bands for Cell-Pb and Cell-Te, respectively. To Cell-Pb, a large amount of Al diffuses into the silicon layer, narrowing the barrier width and forming heavily doped Ohmic contacts. This greatly reduces R_c, improving efficiency.

In summary, the sintering process of Ag/Al paste can be divided into the following parts: volatilization of organic vehicle in the low and medium temperature range; sintering of Ag powder and etching of AlO_x shell on surface of Al powder by molten glass frit at medium and high temperature range. This process is accompanied by the outflow of molten Al. Meanwhile, the molten mixture of Ag, Al and glass frit flows toward the SiN_x surface and forms Ag/Al–Si contact after etching SiN_x. In sintering process, the interaction between glass frit, Ag, and Al can affect the diffusion of substances, thereby affecting the formation of the Ag/Al–Si interface and ultimately determining the performance of the device. TeO_2 efficiently accelerates the sintering of Ag powder and generates numerous Ag colloids within the glass layer at the Ag/Al–Si interface, having minimal impact on reducing R_c for the p^+ emitter interface in Topcon c-Si solar cells. On the contrary, it is Al, rather than Ag, that plays a crucial role in improving the interface. As depicted in Figure 2, channels still retain within the Ag/Al finger following high-temperature sintering, allowing the molten Al to flow toward the interface. Although TeO_2 in the paste exhibits a robust interaction with Ag powder, pure Al in Al powder is encased by an AlO_x shell, necessitating the disruption of this layer for Al diffusion. However, acceleration of Ag

Table 1. The elements proportion of inorganic oxide components of P-Pb and P-Te.

Sample	B (At %)	Si(At %)	Pb(At %)	Te(At %)
P-Pb	35.1	17.2	47.7	0
P-Te	31.1	15.3	42.4	11.2

powder sintering, caused by TeO_2, leads to a reduction in internal voids within the Ag/Al finger, thereby hindering the diffusion of molten Al. Hence, at the interface of Cell-Pb, there is a significantly higher concentration of Al, which diffuses deeper into the Si layer and achieves a higher content, as evident in Figures 3 and 5. Attributed to the greater quantity of Al at Ag/Al–Si interface, Cell-Pb formed a superior contact (heavily doped) compared to Cell-Te. This superior contact facilitates flow of carriers across the Ag/Al–Si interface, resulting in a higher potential difference, which indicates that Al plays a pivotal role in establishing an optimal contact.

3. Conclusion

In conclusion, PbO-based (TeO_2-free) Ag/Al paste and TeO_2-containing Ag/Al paste were prepared to manipulate the sintering process and interface structure, thereby facilitating studies of the sintering and contact formation process. This work clarifies the influence of Al and Ag in the formation of Ag/Al–Si interface. Notably, the PbO-based Ag/Al paste promotes Al migration toward the Ag/Al–Si interface and diffusion into the Si layer, leading to improved contact. While the addition of TeO_2 in Ag/Al paste enhanced the sintering of Ag powder and formed numerous Ag colloids at the Ag/Al–Si interface, it reduced the amount of Al reaching the interface and diffusing into the Si layer, resulting in higher resistance (R_c). This work provides valuable insights for selecting glass components in Ag/Al paste, emphasizing the importance of elements that have weaker reactivity with Ag but stronger reactivity with AlO_x shell on the surface of Al powder, which in turn promotes the migration of Al to the interface and diffusion into the silicon layer. Additionally, considering the interplay between glass frit and metal powders, the characteristics of Ag and Al powders should also be taken into account to further optimize the Ag/Al paste.

4. Experimental Section

Materials Synthesis: Preparation of Ag/Al paste: the blank Ag/Al paste without glass frit was prepared by mixing 84 wt% Ag powder, 2.6 wt% Al powder, 10.4 wt% organic vehicle (consisting of 3% ethyl cellulose, 5% polyamide wax and 92% (2-Butoxyethoxy) ethyl acetate) and using a homogenizer and a three rolls machine to disperse it thoroughly. PbO-based glass frit (3 wt% in Ag/Al paste, which containing Pb, Si, B) was added to blank Ag/Al paste to prepare PbO-based Ag/Al paste (marked as P-Pb) and TeO_2 powder was added to P-Pb to prepare TeO_2-containing Ag/Al paste (marked as P-Te, with TeO_2 0.5 wt%). The elements proportion of inorganic oxide components of these two pastes were shown in **Table 1**.

The rear Ag paste used in this work is made by commercial materials. A 50 mm × 32 mm c-Si solar cell screen printed board, with 1 main finger (0.7 mm) and 21 fine fingers, was used to prepare front and rear electrodes (shown in Figure S8, Supporting Information). By screen printing and co-firing in a belt furnace (Despatch CF-SERIES), front Ag/Al–Si and rear Ag–Si contacts were formed on the TOPCon silicon wafer (54 mm × 36 mm, which was prepared by 182 mm × 182 mm commercial silicon wafers through laser cutting). The cells were fabricated using P-Pb and the P-Te following similar procedures and were marked as Cell-Pb and Cell-Te, respectively.

Materials Characterizations: The morphology and elemental distribution of the materials and devices were examined by scanning electron microscope (SEM, ZEISS SUPRA-55) with energy dispersive spectroscopy (EDS, OXFORD, X-MaxN TSR and transmission electron microscope (TEM, JEM–3200FS, 300 keV) with EDS (OXFORD, X-max 80). X-ray photoelectron spectroscopy (XPS) measurements were conducted using a Thermo Fisher ESCALAB 250X with a monochromatic Al K X-ray source to obtain the valence states of Al and Ag. Before XPS test, the sample surface was sputtered by Ar^+ ions to clean interference from other substances on the surface.

Device Performance Measurements: The electrical parameters of the cells were measured under one sun, AM 1.5G irradiation from a solar simulator (Abet Technologies Model 11000A Sun 3000 Solar Simulator). The R_c of Ag/Al-Si was measured using Keithley Source-Meter 2602A. The surface potential of the Ag/Al–Si interfaces was measured by using an atomic force microscope (AFM, Dimension Icon, Bruker Co., Germany), with a Kelvin probe force microscopy (KPFM) by using Pt/Ir-coated conducting tips (SCM-Pit). The cross section of Ag/Al fingers were prepared by focused Ion beam (FIB, Thermo Fisher Scios), and elements distribution were tested by EDS (OXFORD, X-max 150). The samples of cells for KPFM measurement were cut into 5 mm × 3 mm pieces using a laser, and then polished by an Ar^+ ion beam milling technique (Leica EM TIC 3X, Leica Microsystems GmbH, Germany).

To further confirm the impact of front contact on electrical performance, TLM was used. The graphical parameters of TLM are shown in Figure S9 (Supporting Information). This fitted curve can be written as the following equation:[2c,10a,20]

$$Y = A + Bx \tag{1}$$

where x is the distance between adjacent fingers.

R_c and ρ_c can be calculated according to the following formula:

$$A = 2R_c \tag{2}$$

$$B = \frac{R_{sh}}{W} \tag{3}$$

$$\rho_c = \frac{A^2 W}{4B} \tag{4}$$

where W is the length of finger.

Statistical Analysis: The resistance unit is uniformly converted to Ω, and the length unit is uniformly converted to mm. The statistical data displayed in the bar chart has undergone the K-S normality test ($p \leq 0.05$). The data are presented as mean ± SD. One-way ANOVA, followed by a Tukey post-hoc test, was carried out between groups. In all comparisons, significance was defined as $p \leq 0.05$. The sample size is 5. Statistical analysis was performed using Origin 2022 Software (OriginLab, Northampton, MA, USA).

Supporting Information

Supporting Information is available from the Wiley Online Library or from the author.

Acknowledgements

The author would thank the support of the Soft Science Research Project of Guangdong Province (No. 2017B030301013), and Guangdong Innovative Team Program (No. 2013N080).

Conflict of Interest

The authors declare no conflict of interest.

Author Contributions

Y.L. performed conceptualization, methodology, investigation, and wrote the original draft; R.Z. performed investigation, reviewed and edited the final manuscript; Z.C. performed investigation, reviewed and edited the final manuscript; Y.L. performed investigation;.C. performed investigation; B.Z. performed data processing; J.C. acquired resources; Y.L. reviewed and edited the final manuscript, and performed Project administration. F.P. performed funding acquisition, project administration, and reviewed and edited the final manuscript.

Data Availability Statement

The data that support the findings of this study are available from the corresponding author upon reasonable request.

Keywords

contact resistance, interface structure, silver/aluminum paste, sintering behavior, TOPCon solar cells

Received: May 14, 2024
Revised: June 9, 2024
Published online: June 23, 2024

[1] C. Battaglia, A. Cuevas, S. De Wolf, *Energ Environ Sci* **2016**, *9*, 1552.

[2] a) D. Yan, A. Cuevas, J. I. Michel, C. Zhang, Y. Wan, X. Zhang, J. Bullock, *Joule* **2021**, *5*, 811; b) A. G. Aberle, *Progress in Photovoltaics* **2000**, *8*, 473; c) D. K. Schroder, D. L. Meier, *IEEE Trans. Electron Devices* **1984**, *31*, 637; d) J. I. Michel, J. Dréon, M. Boccard, J. Bullock, B. Macco, *Prog. Photovoltaics* **2022**, *31*, 380.

[3] Y. S. Li, Z. W. Chen, R. Zhou, W. G. Zhao, M. Li, J. Chen, Z. Y. Huang, J. Liu, Y. H. Li, M. L. Yang, M. H. Yu, D. Zhou, Y. Lin, F. Pan, *Nano Res.* **2023**, *17*, 3189.

[4] a) S. Kröner, F. Kiefer, R. Peibst, F. Heinemeyer, J. Krügener, M. Eberstein, presented at 5th Workshop on Metallization for Crystalline Silicon Solar Cells, ISC Konstanz, Constance, Germany **2014**; b) S. Fritz, M. König, S. Riegel, A. Herguth, M. Hörteis, G. Hahn, *IEEE J. Photovoltaics* **2015**, *5*, 145.

[5] a) X. J. Sun, J. J. Xing, Y. X. Yang, X. Yuan, H. B. Li, H. Tong, *J. Electron. Mater.* **2022**, *51*, 5717; b) T. Aoyama, M. Aoki, I. Sumita, A. Ogura, *AIMS Mater. Sci.* **2018**, *5*, 614; c) G. Xing, W. Chen, Y. Liu, X. Du, *Sol. Energy Mater. Sol. Cells* **2024**, *270*, 112814; d) P. Kumar, M. Pfeffer, B. Willsch, O. Eibl, L. J. Koduvelikulathu, V. D. Mihailetchi, R. Kopecek, *Sol. Energy Mater. Sol. Cells* **2016**, *157*, 200; e) F. Kiefer, J. Krugener, F. Heinemeyer, H. J. Osten, R. Brendel, R. Peibst, *IEEE J. Photovoltaics* **2016**, *6*, 1175; f) T. Urban, M. Heimann, A. Schmid, A. Mette, J. Heitmann, *Energy Procedia* **2015**, *77*, 420.

[6] J. D. Fields, M. I. Ahmad, V. L. Pool, J. Yu, D. G. Van Campen, P. A. Parilla, M. F. Toney, M. F. van Hest, *Nat. Commun.* **2016**, *7*, 11143.

[7] J. C. Zhou, J. L. Zhang, B. W. Lv, *Sol. Energy Mater. Sol. Cells* **2023**, *259*.

[8] a) J. Qin, W. J. Zhang, S. X. Bai, Z. F. Liu, *Appl. Surf. Sci.* **2016**, *376*, 52; b) S. Watanabe, T. Kodera, T. Ogihara, *J. Ceram. Soc. Jpn.* **2015**, *123*, 345; c) S. Choi, S. Cho, J. Lee, D. Y. Jeong, H. Kim, *Metals and Mater. Int.* **2015**, *21*, 686.

[9] a) L. Liang, Z. G. Li, L. K. Cheng, N. Takeda, A. F. Carroll, *J. Appl. Phys.* **2015**, *117*, 215102; b) L. Liang, Z. Li, L. K. Cheng, N. Takeda, R. J. S. Young, A. Carroll, *IEEE J. Photovoltaics* **2014**, *4*, 549; c) M. Lu, K. R. Mikeska, C. Ni, Y. Zhao, F. Chen, X. Xie, Y. Xu, C. Zhang, in *2021 IEEE 48th Photovoltaic Specialists Conference (PVSC)*, IEEE, Fort Lauderdale, FL, USA **2021**, 0954.

[10] a) S. Grover, S. Sahu, P. Zhang, K. O. Davis, S. K. Kurinec, presented at 2020 IEEE 33rd International Conference on Microelectronic Test Structures (ICMTS), IEEE, Piscataway, NJ **2020**; b) A. Goetzberger, R. M. Scarlett, Research & Investigation of Inverse Epitaxial Uhf Power Transistors **1964**; c) H. H. Berger, *J. Electrochem. Soc.* **1972**, *119*, 507; d) H. H. Berger, *Solid-State Electron.* **1972**, *15*, 145.

[11] C. Wang, J. Yu, H. U. Ming-Yu, K. H. Zhang, *J. Alloys Compd.* **2018**, *747*, 966.

[12] Y. L. Yan, M. A. Helfand, C. R. Clayton, *Appl. Surf. Sci.* **1989**, *37*, 395.

[13] a) Y. J. Chen, M. J. Zhang, S. Yuan, Y. Qiu, X. B. Wang, X. Jiang, Z. Gao, Y. Lin, F. Pan, *Nano Energy* **2017**, *36*, 303; b) Y. S. Li, Z. W. Chen, B. Zhang, H. B. Chen, R. Zhou, B. W. Nan, W. G. Zhao, K. Li, B. L. Zhao, Y. G. Xiao, J. Liu, J. Chen, Y. Lin, F. Pan, *Nano Energy* **2023**, *116*, 10; c) B. W. Feng, Y. P. Liu, W. Chen, G. G. Xing, X. Q. Chen, X. L. Du, *Sol. Energy Mater. Sol. Cells* **2023**, *257*, 112381.

[14] W. Wu, C. Chan, M. Lewittes, L. Zhang, K. Roelofs, *Proc. Int. Conf. Crystalline Silicon Photovoltaics* **2016**, *92*, 984.

[15] H. Melle, E. Menzel, J. Zaunert, *Physica Status Solidi* **1970**, *1*, 85.

[16] a) S. Fritz, S. Riegel, S. Gloger, D. Kohler, M. König, M. Hörtheis, G. Hahn, *Pro. Int. Conf. Crystalline Silicon Photovoltaics* **2013**, *38*, 720; b) R. Lago, L. Pérez, H. Kerp, I. Freire, I. Hoces, N. Azkona, F. Recart, J. C. Jimeno, *Progress in Photovoltaics* **2010**, *18*, 20.

[17] H. Kerp, S. Kim, R. Lago, F. Recart, A. Shaikh, *Twentyfirst European Photovoltaic Solar Energy Conference*, Dresden **2006**, p. 892–894.

[18] J. A. Amick, F. J. Bottari, J. I. Hanoka, *J. Electrochem. Soc.* **1994**, *141*, 1577.

[19] T. G. Allen, J. Bullock, X. Yang, A. Javey, S. De Wolf, *Nat. Energy* **2019**, *4*, 914.

[20] Z. Chen, L. Xu, *Acta Energiae Solaris Sinica* **2014**, *35*, 750.